

Quantitative determination of the physical parameters relevant to the thin-film directional solidification of the $\text{CBr}_4\text{--C}_2\text{Cl}_6$ eutectic alloy

J. Mergy ^a, G. Faivre ^a, C. Guthmann ^a and R. Mellet ^b

^a *Groupe de Physique des Solides, CNRS URA 17, Tour 23, Place Jussieu, F-75251 Paris Cedex 05, France*

^b *France Télécom, Centre National d'Etudes des Télécommunications Paris B, Laboratoire de Bagneux, 196 Avenue Henri Ravera, F-92200 Bagneux, France*

Received 17 February 1993; manuscript received in final form 19 July 1993

A relatively large number of physical parameters are involved in the formation of lamellar eutectic patterns in thin-film directional solidification: parameters pertaining to the phase diagram of the alloy, diffusion coefficient in the liquid, solid–liquid and solid–solid surface energies. We present a quantitative determination of all these quantities for the $\text{CBr}_4\text{--C}_2\text{Cl}_6$ eutectic alloy, employing only the thin-film directional-solidification setup. By a study of the experimental steady-state shapes of the growth front, we obtain, in particular, the value of the characteristic length known as the Jackson–Hunt minimum-undercooling wavelength.

1. Introduction

In the thin-film directional solidification of a binary eutectic alloy, a large number of physical properties of the alloy are involved. A quantitative knowledge of these material parameters is needed for the comparison between experiment and theory. If the two solid–liquid interfaces have quasi-instantaneous interface attachment kinetics, the one-sided minimal model of directional solidification is the natural basis for the theory [1–4]. The physical properties of the material appearing in this model are:

- the parameters describing the phase diagram of the alloy in the region of the eutectic plateau;
- the chemical diffusion coefficient in the liquid near the eutectic point;
- the surface energies of the solid–liquid and solid–solid interfaces.

In this article, we present a quantitative determination of all these parameters for the $\text{CBr}_4\text{--C}_2\text{Cl}_6$ eutectic alloy. Jackson and Hunt, a long time ago [5], pointed out the suitability of this transparent system for experimental studies in thin-film directional solidification. Since then, this

alloy has been used by a number of authors, and the just mentioned parameters (except for the diffusion coefficient) have been measured by various methods, in particular by Kaukler and Rutter [6–9]. However, several reasons led us to re-measure them during the course of our recent study of lamellar eutectic patterns in this system [10–14].

First, we had to clarify some questions concerning the reliability of the experiments. In particular, it is not clear, according to the literature [6–9,15–19], whether CBr_4 is chemically stable or not above the melting temperature of the crystal. If it is not, the composition of the melt should change during the course of the experiments, and the growth front should be observed to drift, presumably slowly, but continually, towards the cold end of the sample. On the other hand, it has been emphasized by Laherrere et al. [20] that zone-refined organic crystals generally contain substantial amounts of gaseous impurities (i.e., impurities which are susceptible to precipitate in the liquid as a gas). In other words, the supposed binary alloys used in thin-film directional solidification in reality are (at least) ternary alloys. There

is no reason for the $\text{CBr}_4\text{-C}_2\text{Cl}_6$ alloy to be an exception to this general rule. So, the system we are actually dealing with is a $\text{CBr}_4\text{-C}_2\text{Cl}_6\text{-X}$ alloy, where X stands for the unknown residual gaseous impurity(ies). If the partition coefficient of X is small, this may also give rise to a slow, apparently endless, drift of the growth front. Such a drift has indeed been observed by Cladis et al. in the succinonitrile–acetone system [21], and, as we shall explain below, is also present in the $\text{CBr}_4\text{-C}_2\text{Cl}_6$ system, at least in the planar front regime of dilute (i.e., non-eutectic) samples. Does some chemical reaction taking place in liquid CBr_4 contribute to the slow drift of the front? We present here a study of the directional-solidification initial transient in dilute samples which allows us to answer in the negative. In particular, we find good agreement between the values of the alloy thermodynamical parameters that can be deduced from this study, and those obtained by the more standard differential scanning calorimetry (DSC) technique. No pyrolysis of CBr_4 , nor any other chemical reaction, occurs during our experiments.

Our main purpose, however, concerns the dynamics of the $\text{CBr}_4\text{-C}_2\text{Cl}_6$ system in the eutectic concentration range. We have recently determined the position in the control-parameter space of several instability thresholds of the stationary, symmetrical, lamellar eutectic pattern (designated as the eutectic basic state thereafter) [12–14], and it is useful to know, as accurately as possible, the characteristic material parameters to which such thresholds must be compared. Among these parameters appears the length known as the Jackson–Hunt (JH) minimum-undercooling wavelength. Such a quantity can be either calculated from the above listed parameters, or more directly determined by comparing some observed property of the eutectic patterns with theoretical predictions. The latter method is, at least potentially, much more accurate. We present here results obtained by studying the shape of the growth front in the basic state of the system. The accuracy is $\sim 10\%$ on the above-mentioned wavelength.

The article is organized as follows. In section 2, we present various considerations concerning

the stability of CBr_4 , the purification of the alloy, and the making of the directional-solidification samples. Sections 3 to 5 are devoted to (i) the parameters pertaining to the phase diagram, determined DSC and by a study of the initial transient in dilute samples; (ii) the diffusion coefficient, deduced from the measurement, in dilute samples, of the cellular-instability, or Mullins–Sekerka (MS) threshold velocity [22]; (iii) the surface energies, derived, as mentioned above, from the study of the shape of the eutectic growth front in the stationary basic state. In conclusion, we discuss the meaning of the values thus obtained for the JH minimum-undercooling wavelength in the $\text{CBr}_4\text{-C}_2\text{Cl}_6$ system.

2. Products and samples

2.1. Stability of CBr_4

We obtained direct proof of the thermal stability of CBr_4 by means of the DSC technique. We noticed, as others before us [6], that, if the CBr_4 to be analysed is placed in standard stainless-steel or aluminium capsules, a reproducible DSC melting peak cannot be obtained: only the first DSC run, corresponding to the first melting of the product, gives a significant peak. Obviously, liquid CBr_4 reacts with the metal of the container. We replaced the metallic containers by small glass capsules (≈ 0.4 g), in which the zone-refined and outgassed (see below) CBr_4 is sealed under low argon pressure, care being taken not to heat the product during the sealing. The DSC peak of such samples is reproducible. It is not changed by a 24 h annealing at 120°C .

CBr_4 being stable, the decompositions on melting reported in the literature must have actually been reactions with some chemical agent in contact with it. Some simple experiments (not described here) confirm this conclusion [14]. Liquid CBr_4 slowly reacts with oxidizing agents such as moisten air and glues, these reactions being greatly enhanced by illumination. We therefore avoided, as far as possible, any prolonged contact of CBr_4 with such oxidizing agents. We stored the

zone-refined products under a low pressure of argon and in obscurity.

2.2. Purification

We purified both CBr_4 and C_2Cl_6 in the zone-melting installations of the Centre National d'Etude des Télécommunications (CNET), Bagneux. The products to be purified are melted, poured into a glass tube (diameter 1 cm and length 1.4 m), cooled down to room temperature and sealed under a low pressure of argon. The zone-melting apparatus contains 18 annular ovens. During a zone-refining cycle, the tube is pulled over the separation distance of the ovens (pulling velocity $14 \mu\text{m s}^{-1}$), and then rapidly pushed back to its initial position. More than a hundred cycles were given to each tube. The decomposition products of CBr_4 have a typical reddish colour. At the end of the zone-melting process, these coloured products are concentrated in the lower part of the tube. The products used in the experiments come from the white, central part of the tubes.

Zone-refining was also applied to mixtures of about 90 mol% CBr_4 and 10 mol% C_2Cl_6 , the outcome then being a purified eutectic alloy of global concentration very close to the exact eutectic concentration ($C_E \approx 11.8 \text{ mol\%}$ [5]).

2.3. Outgassing

In order to reduce, as far as possible, the concentration of unknown residual gaseous impurities, we outgassed the zone-refined CBr_4 and C_2Cl_6 following a technique similar to that used by Laherrere et al. [20]. The efficiency of this process will be discussed below together with the initial transient in dilute samples, but can also be directly visualized as follows. The high-temperature solid phases of CBr_4 and C_2Cl_6 are plastic, cubic crystals. During directional solidification, no bubble nucleates in the freshly formed high-temperature solid. Bubbles only appear when the solid transforms, at about 50°C , to phases with lower symmetry and higher density. On this transformation, two types of bubbles or voids appear. Small bubbles, which are essentially filled with

the dissolved gas, nucleate in the bulk of the sample. Larger voids form by detachment of the solid from the enclosing glass walls. These are likely to be mostly filled with the ambient air. It can be seen with the microscope that, after this transformation has taken place, non-outgassed samples contain a large density of gas bubbles of both origins, while, in the outgassed samples, the density of bulk-nucleated bubbles is much lower. Clearly, the outgassing process eliminates a significant part, but not all, of the unknown gaseous impurities.

2.4. Samples

The directional-solidification stage is sketched in fig. 1. The details about this stage, given elsewhere [19], will not be repeated here. The sample is pulled at velocity V in a fixed thermal gradient G applied along the z axis. The glass cells containing the alloy are made as sketched in fig. 2a. Two glass plates (0.3 mm thick) are separated by two strips of polyester and held together by an epoxy glue deposited along their edge. During the hardening of the epoxy glue, a strong pressure is applied on the top glass plate. The polyester strips then act as seals, and contact between the glue and the alloy is avoided. The heated cell is filled by capillarity, and then cooled down to room temperature. Since this process is a rapid one, it was done in the air. The useful

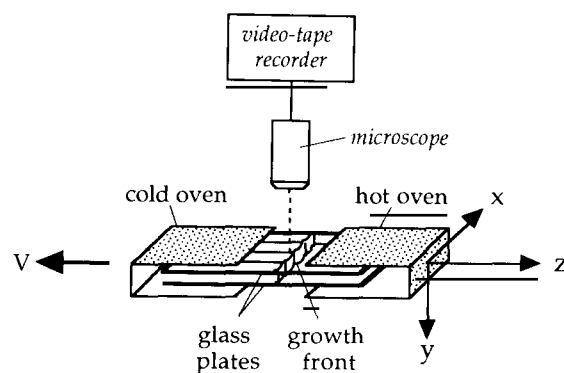


Fig. 1. Sketch of the thin-film directional-solidification setup: z , growth direction; x , lateral direction; y , transverse direction; V , pulling velocity.

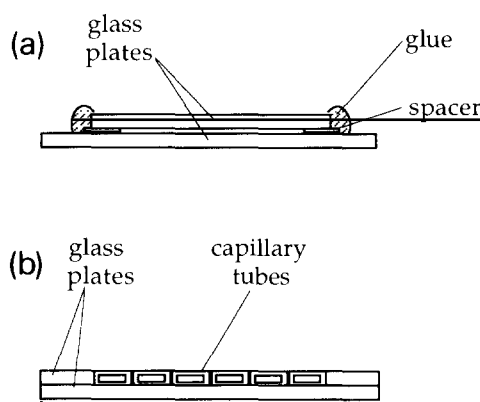


Fig. 2. Transverse cross-section of the two types of experimental cells used in this study (sketch).

width of the cell is about 12 mm. The thickness (determined by the thickness of the polyester spacers) was $12\ \mu\text{m}$ in the present study. In such very thin samples, there is no convection in the liquid, as can be verified with the microscope by observing particules in suspension in the liquid [19].

The main sources of error perturbing the study of the initial transient in dilute samples are the presence of the unknown impurity X and the fact that the temperature distribution along the sample takes some time ($\sim 30\ \text{s}$) to re-stabilize at the onset of the pulling [19]. These difficulties are partly overcome in experimental cells of the type sketched in fig. 2b. These are made of several parallel capillary tubes (microslides tubes, internal cross-section $0.4 \times 0.05\ \text{mm}$), which can be observed simultaneously with the microscope. The use of several tubes filled with the same product allows one to check the lateral homogeneity of the temperature distribution, and to compensate for the possible slight variability of the thermal contacts in the hot oven. On the other hand, comparing the position of the front in capillaries filled with different products (namely, the alloy to be studied and undoped CBr_4) allows one to remedy, to a certain extent, for the above-mentioned perturbative effects.

3. Phase diagram

3.1. DSC

The DSC measurements were performed with a Setaram-DSC 111 apparatus, with the product to be analysed put in sealed glass capsules (see above). The width of the DSC peak of as-purified CBr_4 , as well as that of the zone-refined eutectic alloy, are not significantly larger than that of indium standards. We find the melting temperature of CBr_4 at $T_m = 92.5 \pm 0.3^\circ\text{C}$ and the eutectic temperature at $T_E = 84.4 \pm 0.3^\circ\text{C}$.

A series of alloys were made by mixing together the zone-purified CBr_4 , C_2Cl_6 and the eutectic mixture. The corresponding DSC results are plotted on a phase diagram in fig. 3. The two solid phases at the edges of the eutectic plateau are denoted α and β . A linear fit on the results gives, by extrapolation:

$$C_\alpha \cong 0.088, \quad C_\beta \cong 0.185,$$

with a relative uncertainty about 5%. The composition at the eutectic point ($C_E \cong 0.118$) has not been re-measured, and is taken from ref. [5]. The

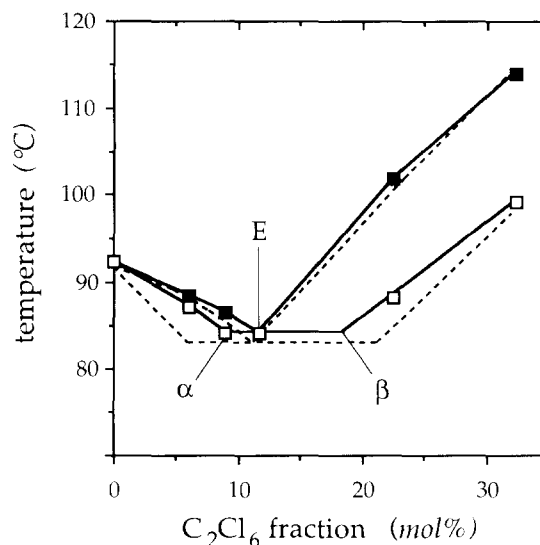


Fig. 3. Phase diagram of the CBr_4 - C_2Cl_6 alloy, as deduced from DSC measurements. Squares and solid lines: this study. Broken lines: after Kaukler and Rutter [8].

enthalpies of melting per unit mass deduced from the areas of the DSC peaks are

$$L_\alpha = 9.5 \pm 0.5 \text{ kJ/kg}, \quad L_\beta = 12.5 \pm 0.5 \text{ kJ/kg}.$$

The liquidus slopes and partition coefficients (i.e., the ratios of the slopes of the liquidus and the solidus) averaged over the explored ranges are

$$m_\alpha = 81 \pm 5 \text{ K mol}^{-1}, \quad K_\alpha = 0.75 \pm 0.1,$$

$$m_\beta = 165 \pm 10 \text{ K mol}^{-1}, \quad K_\beta = 1.5 \pm 0.3.$$

Apparently, m_α and K_α increase as C increases from 0 to C_α . It is, however, not clear whether this increase is significant or not.

The former DSC results of Kaukler and Rutter [8] are shown in fig. 3 for comparison. Apart from a slight overall shift in the temperature scale, a noticeable discrepancy appears as regards the partition coefficient on the CBr₄-rich side (the average value of K_α given by Kaukler and Rutter is 0.42). The measurements presented in the next section were performed, in part, to cross-check this result.

3.2. Initial transient

The initial solute redistribution in directional solidification is a familiar phenomenon. We recall that [23]:

- In a well-homogenized sample of a binary alloy at rest ($V = 0$), the solid–liquid front sits at the temperature T_{liq} corresponding to the liquidus at the overall concentration of the alloy C .
- Under a constant pulling velocity V lower than the MS threshold V_{MS} , the stationary temperature of the front is that of the solidus for the same concentration, T_{sol} . So, during the initial transient, the front recoils toward the cold end of the sample over the distance l_{th} (known as the thermal length) given by:

$$l_{\text{th}} = \frac{T_{\text{liq}} - T_{\text{sol}}}{G} = \frac{m(K^{-1} - 1)C}{G}, \quad (1)$$

where m is the absolute value of the liquidus slope and K the partition coefficient.

- The characteristic duration time of this transient is $\tau = D/V^2$ (where D is the chemical

diffusion coefficient of the solute in the liquid) when K is close to 1, and τ/K when K is much smaller than 1.

- In a dilute ternary alloy, the recoil in the stationary state is merely the sum of the recoils that would be caused by each component separately.

The experimentally measured quantity is the position $z(t)$ of the front in the laboratory frame as a function of time, the zero time being the moment when the pulling motor is switched on. The measurements were made in the above-described capillary cells, the positions of the front being simultaneously recorded in two capillaries, one filled with a non-eutectic CBr₄-rich alloy, the other with undoped CBr₄. Several measurements were made for each concentration. The thermal gradient was calibrated using an empty glass-plate cell in which a thin thermocouple was embedded ($G \cong 85 \pm 3 \text{ K cm}^{-1}$).

The $z(t)$ curves for the capillaries containing the C₂Cl₆-doped CBr₄ clearly present three stages: the instrumental transient extending over the first 30 s or so, a stage essentially controlled by the rejection of C₂Cl₆ lasting a few τ (taking for D the value given in section 4), and a final, roughly linear, stage which does not end for the longest pulling time we used so far ($\sim 20 \tau$). We shall not discuss here in detail the characteristics of this long-lasting final recoil, nor the exact shape of the C₂Cl₆-controlled stage. Complementary observations on these points are currently in progress and will be published later. For our present purpose, it is, however, needful to mention the following observations (S. Akamatsu, unpublished results):

- (1) A long-lasting final recoil is also found, with the same general characteristics, in the capillaries filled with undoped CBr₄.
- (2) The final recoil can be quantitatively characterized by the average slope of the $z(t)$ curves in the corresponding region. This slope does not prove to be a well-reproducible quantity. Statistically, however, it shows no systematic variation with C , but seems roughly proportional to V ($V^{-1}dz/dt \sim 10^{-2} \text{ s}$).
- (3) Gas bubbles can be made to nucleate in the liquid at the growth front, for instance by sud-

denly increasing the pulling velocity during the course of the final recoil.

(4) When the pulling is stopped, the front returns to its initial position at rest.

(5) For eutectic fronts, no slow drift has been detected.

Observations 1 to 3 are consistent with the fact that the final recoil is essentially due to an ill-controlled gaseous impurity. Observation 4 shows that this impurity is not the result of a chemical reaction taking place during the pulling. The discussion of observation 5 is beyond the scope of the present article, but it shows that we can reasonably ignore the effect of residual gases when we study the eutectic basic state studied in section 5.

A concentration of $\sim 10^{-4}$ and a partition coefficient of ~ 0.1 for the residual gas would be compatible with the observed slope of the final recoil. These values, compared with that of the undoped-sample MS threshold given below ($\sim 25 \mu\text{m s}^{-1}$), lead to the reasonable value of $\sim 160 \text{ K}$ for the $\text{CBr}_4\text{-X}$ liquidus slope.

The various stages of the $z(t)$ curves being identified, the next step is to extract the C_2Cl_6 -controlled recoil from the other components. No rigorous way of doing that being yet available, we merely subtracted the $z(t)$ curve corresponding to the capillary filled with undoped CBr_4 from that corresponding to the doped CBr_4 . The resulting recoil curve saturates after a few τ to a value which we took as being the thermal length defined by eq. (1). The corresponding results are given in fig. 4. It is seen that the agreement with our DSC results is reasonable, especially with regard to the value of K_α .

It is also worth noting that we did not find the amplitude of the C_2Cl_6 -controlled recoil to vary with the pulling velocity, which confirms that, for the pulling velocities used here, the interface attachment kinetics is quasi-instantaneous.

4. Diffusion coefficient

The MS threshold velocity is given, to a good approximation [24], by:

$$V_{\text{MS}} = D/l_{\text{th}}, \quad (2)$$

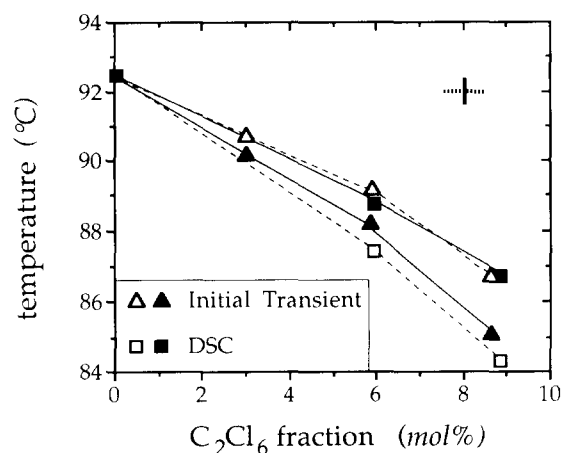


Fig. 4. CBr_4 -rich side of the phase diagram. Triangles and broken lines: results deduced from the study of the recoil of the front during the initial transient. Squares and solid lines: as in fig. 3.

where D is the diffusion coefficient of the solute in the liquid and l_{th} the thermal length given by eq. (1). If the recoil l_{th} and the de-stabilization threshold V_{MS} are measured in the same sample, D can be obtained from eq. (2), the result not being affected by the uncertainty of the value of C . We performed such coupled measurements for a series of CBr_4 -rich alloys, including undoped CBr_4 . The procedure is to begin pulling the sample with a velocity somewhat lower than V_{MS} , wait for the planar front to stabilize at T_{sol} , and then increase V by small steps, waiting some definite time ($\sim 0.5 \text{ h}$) after each increase of V , until some deformation of the planar front appears. To avoid large finite-size effects, the observations were made in the wide glass-plate cells. The results obtained are reported in fig. 5, where V_{MS}^{-1} is plotted as a function of l_{th} . Several measurements were performed for each concentration, and the error bars represent the experimental scatter. A linear fit on the experimental data gives

$$D = (0.5 \pm 0.1) \times 10^{-5} \text{ cm}^2 \text{ s}^{-1}.$$

This is indeed the order of magnitude expected for a diffusion coefficient in the liquid phase.

The value appearing in fig. 5 at $l_{\text{th}} = 0$ is that found in undoped CBr_4 samples by applying the

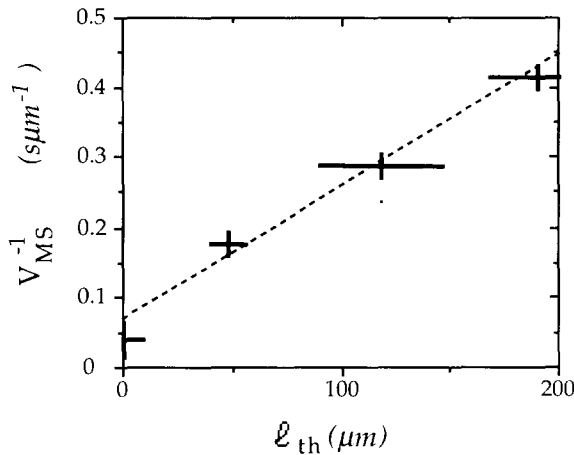


Fig. 5. Inverse cellular-instability (MS) velocity versus corrected (see ref. [38]) thermal length, for various alloy concentrations. Broken line: numerical fit.

just described procedure. It is certainly much above the real V_{MS}^* of the $\text{CBr}_4\text{-X}$ alloy. As mentioned above, this alloy has a very small value of its partition coefficient, so that the transients following the velocity jumps are long, in fact much longer than the stabilization time we actually applied. This question will be discussed in detail in another article, currently in preparation.

5. Surface energies

Three material parameters appearing in the minimal model of eutectic solidification remain to be determined: the energies of the α -liquid, β -liquid and α - β interfaces, respectively noted γ_α , γ_β and $\gamma_{\alpha\beta}$ hereafter. The model, in its usual form, does not take capillary anisotropy (i.e., the fact that these energies actually vary with the orientations of the interfaces with respect to the crystal lattices) into account. The role played by capillary-anisotropy effects has been discussed elsewhere [11]. Their strength depends on the relative orientation of the two crystal phases, and is therefore different in different eutectic grains. In our system (and, most probably, in all “regular” eutectics), most eutectic grains are of the “floating” type, and capillary-anisotropy effects are weak. This shows up, experimentally, as fol-

lows. Capillary anisotropy breaks the reflection-symmetry of the pattern, which then drifts laterally along the front. Consequently, the lamellae left behind in the solid are tilted with respect to the growth direction. A large tilt angle means a strong capillary anisotropy, and, in general, a small tilt angle means a weak anisotropy. For the present study, we selected eutectic grains with undetectable ($< 0.5^\circ$) anisotropy-driven tilt angles, and assumed that, in such grains, capillary anisotropy is negligible. More precisely, we admit that the weakly orientation-dependent surface energies can be replaced by their orientation-independent average values. This does not mean that the orientation, and hence the average surface energies, were the same in all the grains selected. Some variability of the results from grain to grain is therefore to be expected.

Basically, the method described in this section consists of fitting the calculated front profiles to the experimental ones, with the unknown surface energies used as the adjustable parameters of the fitting. Such a method obviously implies that a large number of profiles can be computed. Therefore, although it is possible to integrate, numerically, the equations of the minimal model with high-speed computers [25], we contented ourselves with the approximate calculation method of Jackson and Hunt [2]. The conditions under which this approximation is valid have long remained uncertain, but this was recently cleared up by Brattkus, Caroli, Caroli and Roulet [27]. These authors point out the presence, in the initial calculation by Jackson and Hunt, of an unnecessary simplifying assumption (the “equal-undercooling ansatz”; see appendix for details), which they remove. Then, they show that the ansatz-freed JH approximation is a satisfactory one under certain conditions (specified below), which we shall show to be reasonably fulfilled in our experiments.

In order to introduce the appropriate reduced variables, we must briefly recall how the JH approximation works. There are 4 experimental variables in the problem: G , V , C and the wavelength λ of the pattern. Let us consider the system in the basic state at fixed values of these variables (fig. 6). Along the growth axis z , the

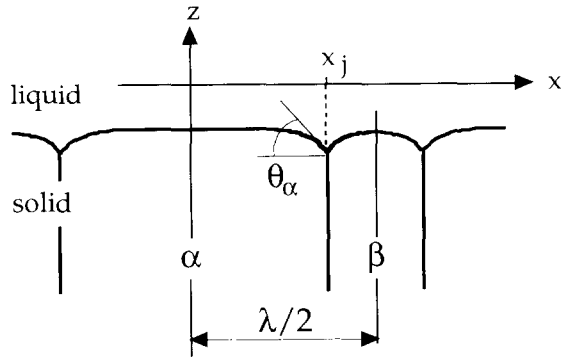


Fig. 6. Reference frame and notations for the calculation of the front profile in the basic steady state (see text). The origin along the z axis is at $T = T_E$.

origin is taken at the point where $T = T_E$. Along the lateral axis x , for symmetry reasons, it will suffice to consider the interval $0 \leq x \leq \lambda/2$. Within it, the front is formed by two segments, corresponding, in the solid, to half an α and half a β lamella, respectively. These segments join at a triple point located at

$$x_j = \eta_\alpha/2, \quad (3)$$

where η_α is the volume fraction of the α phase in the solid, given by (in the JH approximation):

$$\eta_\alpha = (C_\beta - C)/\Delta C, \quad (4)$$

where $\Delta C = C_\beta - C_\alpha$. The contact angles θ_α and θ_β of the two segments at the triple points are fixed by the equilibrium Young conditions. The unknown front profile $z(x)$, its curvature $\mathcal{K}(x)$ and the unknown concentration field at the interface are linked together by the Gibbs–Thomson equation.

The Gibbs–Thomson equation for the α –liquid interface reads:

$$T_E - T(x) = -Gz(x) = m_\alpha [C(x) - C_E] - a_\alpha \mathcal{K}(x), \quad (5)$$

where

$$\mathcal{K}(x) = z_{xx}/(1 + z_x^2)^{3/2}, \quad (6)$$

$$a_\alpha = \gamma_\alpha T_E / \rho_\alpha L_\alpha. \quad (7)$$

A similar equation can be written for the β –liquid interface. It is common practice to introduce the reduced departure from the eutectic concentration

$$u(x) = [C(x) - C_E]/\Delta C, \quad (8)$$

together with the α thermal and capillary lengths,

$$l_{th,\alpha} = m_\alpha \Delta C / G, \quad (9)$$

$$d_\alpha = \gamma_\alpha T_E / \rho_\alpha L_\alpha m_\alpha \Delta C, \quad (10)$$

where ρ_α is the density of the α solid phase, and write eq. (5) as:

$$-z(x) = l_{th,\alpha} [u(x) - d_\alpha \mathcal{K}(x)]. \quad (11)$$

In eq. (11), both $u(x)$ and $z(x)$ are unknown functions. The JH approximation essentially consists of replacing $u(x)$ by the approximate analytical formula obtained by assuming the growth front to be perfectly flat:

$$u_{JH}(x) = u_0 + \frac{\lambda P(\eta_\alpha)}{l_{diff}} \left[F\left(\eta_\alpha \frac{x}{\lambda}\right) + \frac{1}{\eta_\alpha} \right]. \quad (12)$$

We need not concern ourselves here with the X -independent term u_0 , which turns out to be eliminated later on. $P(\eta_\alpha)$ is the value of the function

$$P(\eta) = \sum_{p \geq 1} \frac{\sin^2(\pi p \eta)}{\pi^3 p^3} \quad (13)$$

for $\eta = \eta_\alpha$. The function F is defined in terms of the same function by

$$F(\eta, X) = \frac{2}{P(\eta)} \left[P'\left(\frac{\eta}{2} + X\right) + P'\left(\frac{\eta}{2} - X\right) \right] - \frac{1}{\eta}. \quad (14)$$

Plots of $P(\eta)$ and $F(\eta, X)$ are given in figs. 14 and 15 of the appendix. Note that $P(\eta_\alpha) \sim 10^{-2}$, while $\langle F(\eta_\alpha, X) \rangle_\alpha = 0$ and $F(\eta_\alpha, 0) \sim 1$.

Substituting (12) into (11) leads to a second-order differential equation for $z(x)$, with known

variable coefficients. Performing the change of variables:

$$X = x/\lambda, \quad (15)$$

$$Z(X) = [z(x) - \langle z(x) \rangle_\alpha] / \lambda, \quad (16)$$

where $\langle \rangle_\alpha$ denotes the average taken over the interval $(0, x_j)$, we finally obtain the dimensionless equation

$$\frac{Z_{XX}}{(1 + Z_X^2)^{3/2}} = -K_\alpha \left\{ 1 - \Lambda_\alpha \left[\frac{\Gamma_\alpha}{P(\eta_\alpha)} Z + F(\eta_\alpha X) \right] \right\}, \quad (17)$$

where

$$\langle K(X) \rangle_\alpha = -K_\alpha = -2 \sin(\theta_\alpha) / \eta_\alpha, \quad (18)$$

$$\Gamma_\alpha = GD / Vm_\alpha \Delta C, \quad (19)$$

$$\Lambda_\alpha = \lambda^2 VP(\eta_\alpha) / Dd_\alpha K_\alpha. \quad (20)$$

The (reduced) profile of the α -liquid interface, $Z(X)$, is the solution of eq. (17) obeying the boundary conditions

$$Z_X(X=0) = 0, \quad (21)$$

$$Z_X(X=X_j) = -\tan(\theta_\alpha). \quad (22)$$

It is seen in eq. (17) that, of the 4 experimental variables, only η_α and the two quantities $\lambda^2 V$ and G/V come into play, in conformity with the similarity laws established by Kassner and Misbah [26]. The characteristic constants fixing the significant orders of magnitude for $\lambda^2 V$ and G/V are

$$(\lambda^2 V)_{\text{scal},\alpha} = K_\alpha d_\alpha D / P(\eta_\alpha), \quad (23)$$

$$(G/V)_{\text{scal},\alpha} = m_\alpha \Delta C / D. \quad (24)$$

These quantities, and the similar ones for the β lamellae, are those which we actually determine when we adjust the calculated profiles on the experimental ones. Considering eq. (23) as defining a characteristic length for the α lamellae, $\lambda_{\text{scal},\alpha}$, which varies with V as $V^{-1/2}$, and introducing the diffusion length

$$l_{\text{diff}} = D/V, \quad (25)$$

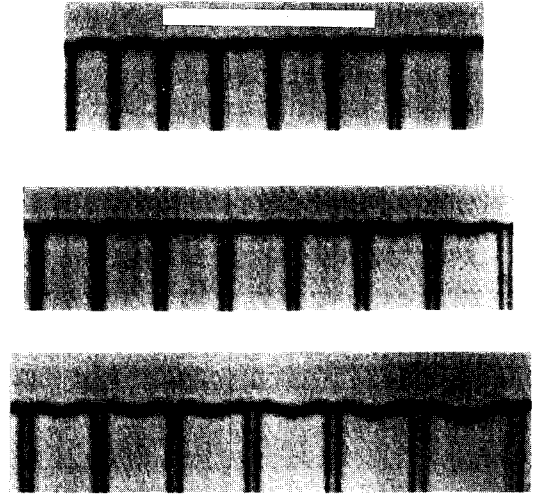


Fig. 7. A region of the growth front showing a permanent λ gradient. $\eta_\alpha \approx 0.88$; $G \approx 80 \text{ K cm}^{-1}$; $V \approx 1.36 \text{ } \mu\text{m s}^{-1}$. The evaluated value of λ_{scal} is $19 \text{ } \mu\text{m}$. In this region, λ ranges from 22 to $43.7 \text{ } \mu\text{m}$, and thus Λ from 1.3 to 5.3 . $\Gamma \approx 0.28$. Marker represents $100 \text{ } \mu\text{m}$.

we obtain the expressions

$$\lambda_{\text{scal},\alpha} = (K_\alpha l_{\text{diff}} d_\alpha / P(\eta_\alpha))^{1/2}, \quad (26)$$

$$\Gamma_\alpha = l_{\text{diff}} / l_{\text{th},\alpha}. \quad (27)$$

Before turning to the numerical results, it is useful to describe qualitatively the general features of the solutions to eq. (17), in view of the existence, in the eutectic basic state, of permanent gradients of the local wavelength. An illustrative example is shown in fig. 7. The origin of such gradients and the meaning of their persistence have been explained elsewhere [11]. The evolution of the front profile as a function of λ , at fixed V , G and C , can be qualitatively understood as follows. The second and third terms on the right-hand side of eq. (17) express, respectively, the effects of the thermal gradient and the concentration field. Both are proportional to Λ_α , while Γ_α (which does not depend on λ) measures their relative weight. For $\Lambda_\alpha = 0$, the solution of eq. (17) is simply a circular arc. For $0 < \Lambda_\alpha \ll 1$, the deviation of the solution from the circular shape is essentially a slight flattening near the tip, to which, since $F(\eta_\alpha, 0)$ and $Z(0)$ are positive, both the gradient and the concentration terms

contribute. On the other hand, for a sufficiently large value of A_α , the curvature at $X=0$ is positive, and the lamella presents a trough at its tip. The depth of the trough increases as A_α increases. However, when the trough is deep enough for $Z(0)$ to be negative, the gradient term acts against a further deepening of the trough. The value A_{inv} at which the curvature at the tip changes sign can be taken as the boundary between the two qualitatively different types of profiles. A_{inv} is of order 1 as long as Γ_α is not much larger than 1.

Let us now turn to the quantitative results. The measurements performed cover the concentration range corresponding to $0.5 \leq \eta_\alpha \leq 0.88$, and the velocity range $0.25 \leq V \leq 2.5 \mu\text{m s}^{-1}$, with G fixed at a value close to 80 K cm^{-1} . The procedure is as follows. In a given sample, and for a given pulling velocity, a eutectic grain with a small capillary anisotropy is selected. Images of the front in this grain are recorded in several regions with different λ , but with a low λ gradient. (The latter condition comes into play because a gradient of λ means a breaking of reflection symmetry of the front profile. In practice, however, this effect is very weak, and the condition is not a stringent one.) λ and η_α are then measured for each pair of lamellae. The instrumental error on λ is $\sim 0.5 \mu\text{m}$, and λ is typically $20 \mu\text{m}$. Thus, the instrumental error on η_α is ~ 0.03 . The spatial variations of η_α do not significantly exceed 0.03, indicating that the average concentration is uniform along the growth front, in spite of noticeable variations of λ .

The next step is then to deduce, for each type of lamella, the value of the unknown material parameters from the shape of the corresponding solid-liquid interfaces. Let us, as before, consider the α -liquid interfaces. On each lamella, we measure the morphological variable (see fig. 8):

$$H = [Z(0) - Z(X_j)]/X_j. \quad (28)$$

Note that the value of H at $\lambda = 0$ depends only of θ_α , not on d_α :

$$H(\lambda = 0) = \tan(\theta_\alpha/2).$$

Moreover, H decreases monotonically with in-

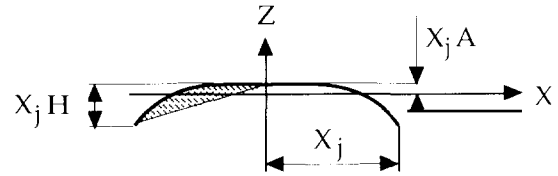


Fig. 8. The two morphological variables A and H (see text). The shaded area is equal to $H - 2A$. The origin along the Z axis is such that $\langle Z \rangle_\alpha = 0$.

creasing λ (at least, as long as $Z(0) > 0$). One thus obtains, for a given experimental run, a series of values of the function $H(\lambda^2 V)$, at given values of C , G and V . A numerical fit to these experimental data then gives θ_α and d_α .

An example is shown in fig. 9, where two series of experimental data are plotted, corresponding to the same alloy ($\eta_\alpha \cong 0.62$), at two different pulling velocities (0.27 and $1.54 \mu\text{m s}^{-1}$; V is known to within $\sim 3\%$), and in two different eutectic grains. In fact, to increase the accuracy with which θ_α and d_α are determined, the data on which the fit was performed include the values of a second morphological variable, also defined in fig. 8:

$$A = Z(0)/X_j. \quad (29)$$

It is seen that the numerical best fits for the two

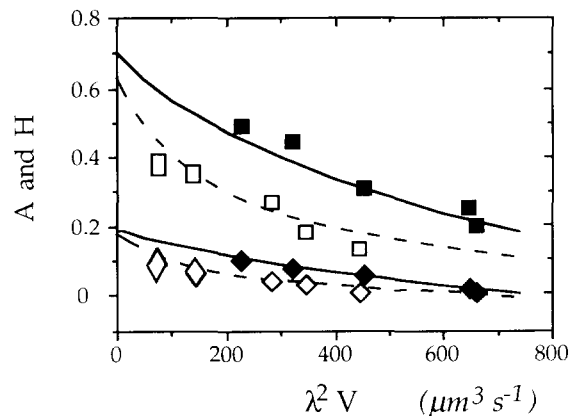


Fig. 9. Measured values of H (solid symbols) and A (open symbols) for the same sample as in fig. 8 ($\eta_\alpha \cong 0.62$; $G \cong 80 \text{ K cm}^{-1}$). Squares: $V \cong 1.54 \mu\text{m s}^{-1}$ ($\Gamma = 0.25$). Lozenges: $V \cong 0.27 \mu\text{m s}^{-1}$ ($\Gamma \cong 1.4$). Curves: numerical fits.

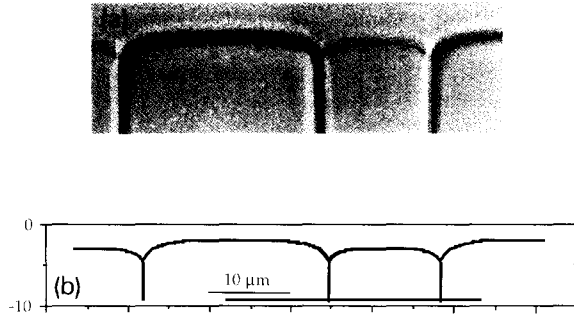


Fig. 10. Comparison between basic-state front profiles: (a) observed; (b) calculated for the values of the material parameters given in the text. $\eta_\alpha \approx 0.62$; $G \approx 80 \text{ K cm}^{-1}$; $V \approx 0.27 \mu\text{m s}^{-1}$; $\lambda \approx 37 \mu\text{m}$ ($A \approx 2.0$, $\Gamma \approx 1.4$). The optical image has been digitalized, thresholded and vectorized in order to obtain, for the front profile, the line visible in (a).

series of data do not intercept the vertical axis exactly at the same point: in other words, they give two slightly different values of θ_α (65° and 70° , respectively) for practically the same value of d_α (10.5 nm). This can be attributed either to the different orientations of the two grains, or to the different values of V leading to a different deviation of the JH approximation from the exact solution of the model. We shall return to this point below.

Other samples, with different concentrations, gave the same result, with a similar scatter. The same procedure, applied to the β lamellae, gives a larger uncertainty on θ_β and d_β , for the reason, principally, that the β -liquid interfaces have a

poorer contrast of their optical images than the α -liquid ones. The Young conditions can then be utilized to restrict the allowed range of values for θ_β and d_β . Finally, the values

$$\theta_\alpha = 70 \pm 4^\circ, \quad d_\alpha = 10.5 \pm 0.8 \text{ nm},$$

$$\theta_\beta = 67 \pm 5^\circ, \quad d_\beta = 35 \pm 0.5 \text{ nm},$$

give quite satisfactory fits for $0.5 \leq \eta_\alpha \leq 0.8$, as shown by figs. 10 and 11. Only for $\eta_\alpha \approx 0.88$ and for the highest values of λ does an appreciable discrepancy between calculated and observed profiles appear: the trough at the tip of the calculated profiles is not as deep as in the observed one.

The above uncertainties amount, in relative value, to $\sim 8\%$. We stress again that this actually represents the uncertainty of the values of the characteristic quantities defined by eqs. (23) and (24) for the α lamellae, and by similar equations for the β lamellae. Ultimately, however, we are interested in the dimensionless control variables and characteristic quantities for the *pairs* of lamellae. These are defined by [2]:

$$A = \lambda^2 V / (\lambda^2 V)_{\text{scal}} = (\lambda / \lambda_{\text{scal}})^2, \quad (30)$$

$$\Gamma = l_{\text{diff}} / l_{\text{th}}, \quad (31)$$

$$(\lambda^2 V)_{\text{scal}} = \eta_\alpha \eta_\beta [(\lambda^2 V)_{\text{scal},\alpha} + (\lambda^2 V)_{\text{scal},\beta}] / 2, \quad (32)$$

$$l_{\text{th}}^{-1} = (l_{\text{th},\alpha}^{-1} + l_{\text{th},\beta}^{-1}) / 2, \quad (33)$$

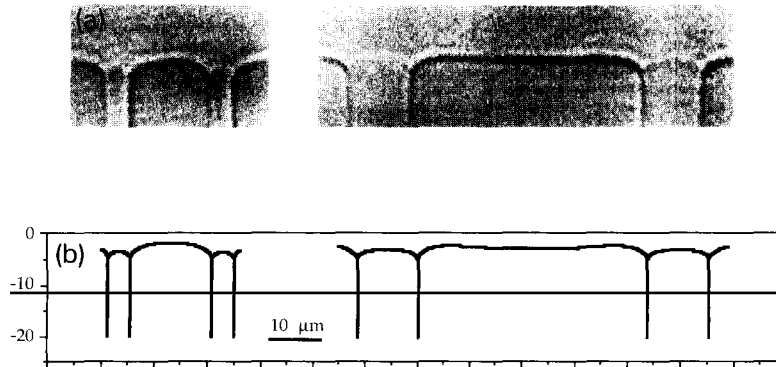


Fig. 11. (a) Observed; (b) calculated basic-state front profiles. $\eta_\alpha \approx 0.79$; $G \approx 80 \text{ K cm}^{-1}$; $V \approx 0.27 \mu\text{m s}^{-1}$; $\lambda \approx 19.7$ and $56.3 \mu\text{m}$ ($A \approx 0.4$ and 3.2 , $\Gamma \approx 1.4$).

where $\eta_\beta = 1 - \eta_\alpha$. Taking into account the uncertainty of G and V , we estimate the order of magnitude of the relative uncertainty on the global scaling parameters to be 15–20%. This includes the scatter due to the grain-dependence of the surface energies.

The surface energies, calculated by assuming the unknown densities ρ_α and ρ_β to be equal to the known density of pure CBr_4 ($\approx 3 \text{ g cm}^{-3}$), are:

$$\gamma_\alpha \approx 6.6 \times 10^{-3} \text{ J m}^{-2}, \quad \gamma_\beta \approx 5.8 \times 10^{-3} \text{ J m}^{-2},$$

$$\gamma_{\alpha\beta} \approx 11.5 \times 10^{-3} \text{ J m}^{-2}.$$

The values found for γ_α and γ_β , and the fact that $\gamma_\alpha \approx \gamma_\beta$, are in good agreement with the empirical correlation laws established by Turnbull and coworkers [28]. They are also in rough agreement with results of Kaukler and Rutter, obtained by a different method [7]. The α -liquid interface has a much greater apparent “stiffness” than the β -liquid one ($d_\alpha/d_\beta \approx 3$), mostly because of the difference between the liquidus slopes ($m_\beta/m_\alpha \approx 2$). Noteworthy additional, qualitative evidence of the latter property is given by the shape taken up by the growth front in the so-called tilted state. Without entering into details (given elsewhere [13]), we recall that, in addition to the branch of symmetrical (basic) states, the system admits a branch of stationary asymmetrical drifting, or tilted, states. Fig. 12 shows the shape of the growth front in such a tilted state near the middle of the eutectic plateau, i.e., when α and β lamellae have approximately the same width. It is clearly seen that most of the deformation of the front profile is borne by the softer β -liquid interfaces.



Fig. 12. Front profile in the stationary tilted state. $\eta_\alpha \approx 0.50$; $G \approx 30 \text{ K cm}^{-1}$; $V \approx 1.54 \text{ } \mu\text{m s}^{-1}$; $\lambda \approx 28 \text{ } \mu\text{m}$. The solid phase with the darker contrast is α . Marker represents $100 \text{ } \mu\text{m}$.

In conclusion of this section, let us briefly discuss the validity of the model used for the calculation. There is good reason to believe that, for our very thin system, the only questionable assumptions we have made are: (i) no capillary anisotropy; (ii) translational invariance in the transverse (see fig. 1) direction; (iii) validity of the JH approximation. Assumption (i) has been discussed above. As for the transverse translational invariance, it is actually broken by the menisci formed by the interface in contact with the glass plates. No direct observation of these menisci as a function of V has ever been performed, to our best knowledge, and a theoretical analysis is also lacking. There is indeed indirect evidence that the menisci at the glass plates play a major role with regard to the transverse instabilities: in very thin samples, these instabilities are efficiently locked [12,13]. However, this does not imply that the deformation of the front shape in the xz plane due to the menisci is a large one. Whatever the meniscus effect is, its relative amplitude is likely to vary in a systematic way with λ and V . The fact is that, if there is a systematic variation of the discrepancy between calculations and experiments with these control parameters, it does not exceed the above-mentioned 8%.

According to Brattkus et al. [27], the JH approximate solution of the model approaches the exact one (transverse translational invariance being assumed for both) for $\lambda/l_{\text{diff}} \ll 1$ (small Péclet number) and $\Gamma \gg 1$. In fact, it has been shown numerically by Kassner and Misbah [25] that the JH front shapes are already quite close to the exact ones when $\Gamma = 2$, at least for $\Lambda \approx 1$. In our experiments, and for $0.5 < \eta_\alpha < 0.8$, $\lambda/l_{\text{diff}} \leq 5 \times 10^{-2}$ and $0.25 \leq \Gamma \leq 2$. So the condition $\Gamma \sim 2$ is not always fulfilled (note that choosing V and G in order to get larger Γ values would not increase the accuracy of the method, since it would entail a pronounced flattening of all profiles). However, Kassner and Misbah have also computed the exact values of H and A as functions of λ for $\Gamma = 0.5$ (private communication), showing that the discrepancy between exact and JH values increases as $\lambda^2 V$ increases, but does not exceed 15% for $\Lambda = 2$. So, by using the JH approximation in the above extrapolation procedure, we

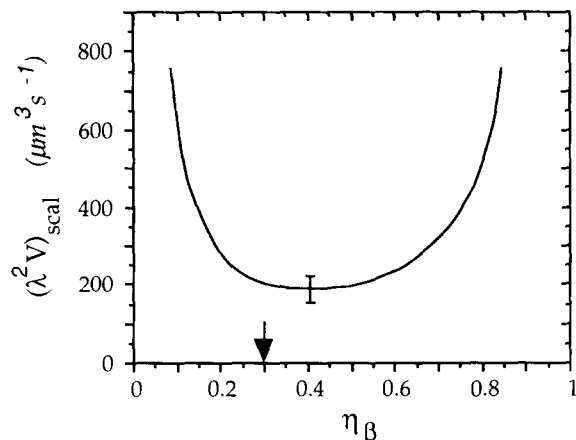


Fig. 13. The parameter $(\lambda^2 V)_{scal}$ as a function of $\eta_\beta = (C - C_\beta)/(C_\alpha - C_\beta)$. Arrow: eutectic point.

overestimated the contact angles by, at most, 15%. As already mentioned, this is one of the possible explanations for the difference between the values of θ_α delivered by the two series of points in fig. 9.

The above-mentioned discrepancy between calculated and observed profiles for $\eta \approx 0.88$ and $\Lambda \geq 2$ can also be explained by the remark made by Kassner and Misbah [25] that, at large Λ , the JH profiles present a less pronounced trough at their tip than the exact ones. That this deviation is only observed near the edge of the eutectic plateau is probably due to the relatively large values of the Péclet number ($\lambda/l_{diff} \sim 0.1$) in this region.

6. Conclusion

The main result of this study, as far as eutectic growth in the $\text{CBr}_4\text{-C}_2\text{Cl}_6$ system is concerned, is the value of the characteristic parameter $(\lambda^2 V)_{scal}$, plotted in fig. 13 as a function of the concentration of the alloy (represented, for convenience, by η_β). Near the centre of the eutectic plateau, the relative uncertainty is only $\sim 20\%$. The Jackson–Hunt minimum-undercooling wavelength λ_{scal} at a given pulling velocity is easily calculated from

the data of fig. 13 (see eq. (30)). In conclusion, we would like to make a few comments about the exact meaning of this important quantity.

Given G , V and C , the average undercooling of the growth front in the basic state is a function of λ presenting a minimum for a certain wavelength λ_{min} . The approximate calculation by Jackson and Hunt, published in 1966, gave $\lambda_{min} = \lambda_{scal}$ [2]. Actually, as mentioned above, λ_{min} is not exactly equal to λ_{scal} . We have calculated λ_{min} for the $\text{CBr}_4\text{-C}_2\text{Cl}_6$ system in the (fully consistent) JH approximation. The calculation and its results are given in the appendix. Contrary to λ_{scal} , which depends on V only, the relative discrepancy between λ_{min} and λ_{scal} depends on the two control parameters V and G . This discrepancy is indeed small, for realistic values of V and G , but not always fully negligible, compared to the uncertainties with which the wavelengths are experimentally determined.

On the other hand, contrary to what has been sometimes conjectured, neither λ_{min} nor λ_{scal} coincides exactly with the marginal-stability wavelength for the pinching-off (or lamellar extinction) instability. A linear stability analysis performed in a particular limit (vanishing contact angles at triple points) shows that the stability range of the basic state is limited, towards small λ , by a value λ_{pinch} close to, but different from λ_{scal} and λ_{min} ($\lambda_{pinch} < \lambda_{min}$) [29]. This result, although only demonstrated in a particular (and unrealistic) case, establishes that λ_{pinch} is, in general, not equal to λ_{min} .

So it seems that no particular physical property is attached to the “JH minimum-undercooling wavelength” λ_{scal} . Indeed, the stable wavelengths of the lamellar eutectic basic pattern are always observed to be rather close to λ_{scal} (see figs. 10 and 11 and refs. [9,13,14,30]). But this only means that λ_{scal} is one of the appropriate characteristic, or scaling lengths of the eutectic problem. The knowledge of λ_{scal} gives the order of magnitude of the pattern wavelength. More precisely, any experimental determination of a wavelength corresponding to a bifurcation or instability threshold of a lamellar eutectic system should be given in λ_{scal} units, in order for the results obtained for different velocities, concen-

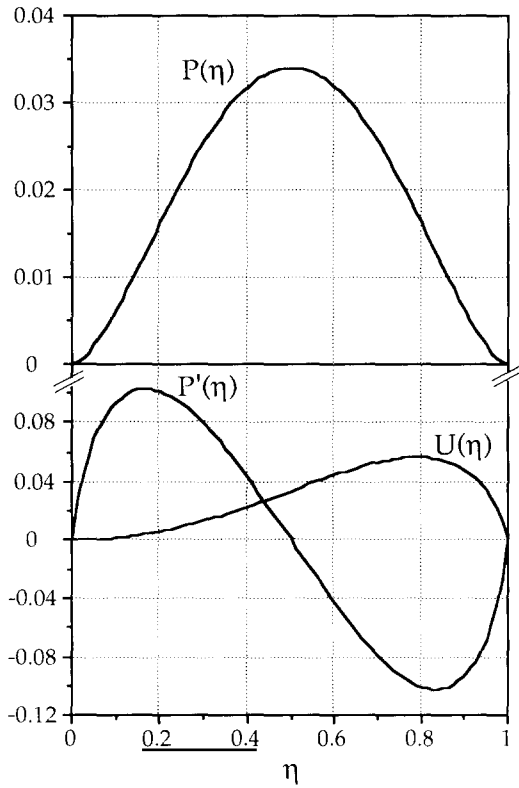


Fig. 14. Various functions defined in the text.

trations and even alloys to be quantitatively compared.

Appendix

The JH function $P(\eta)$ defined by eq. (13) and other useful functions are plotted in figs. 14 and 15. Knowing these functions, we can calculate not only the shape of the front, but also λ_{\min} in the JH approximation. The average undercooling of the front is defined by

$$\langle \Delta T \rangle / G = \eta_\alpha \langle z \rangle_\alpha + \eta_\beta \langle z \rangle_\beta. \quad (A.1)$$

Averaging eq. (12) over the interval $(0, x_j)$ and the corresponding equation for the β lamella over $(x_j, \lambda/2)$, and eliminating the unknown constant u_0 , gives a linear relationship between $\langle z \rangle_\alpha$ and $\langle z \rangle_\beta$. A second linear equation is obtained as follows. Integrating eq. (17) gives the front profile

in the reference frame where $\langle Z \rangle_\alpha = 0$, and similarly for the β lamella. In order to impose, moreover, the continuity of the front profile at x_j , we come back to the unreduced variables x and z , and write

$$z_j = \lambda Z_{j,\alpha} + \langle z \rangle_\alpha = \lambda Z_{j,\beta} + \langle z \rangle_\beta, \quad (A.2)$$

where $Z_{j,\sigma} = Z(X_j)$ for the σ lamella. It is this equation which, in the original calculation by Jackson and Hunt, is replaced by the equal average-undercooling ansatz $\langle z \rangle_\alpha = \langle z \rangle_\beta$. Some straightforward algebra leads to:

$$\langle \Delta T \rangle = \langle \Delta T \rangle_1 + \langle \Delta T \rangle_2, \quad (A.3)$$

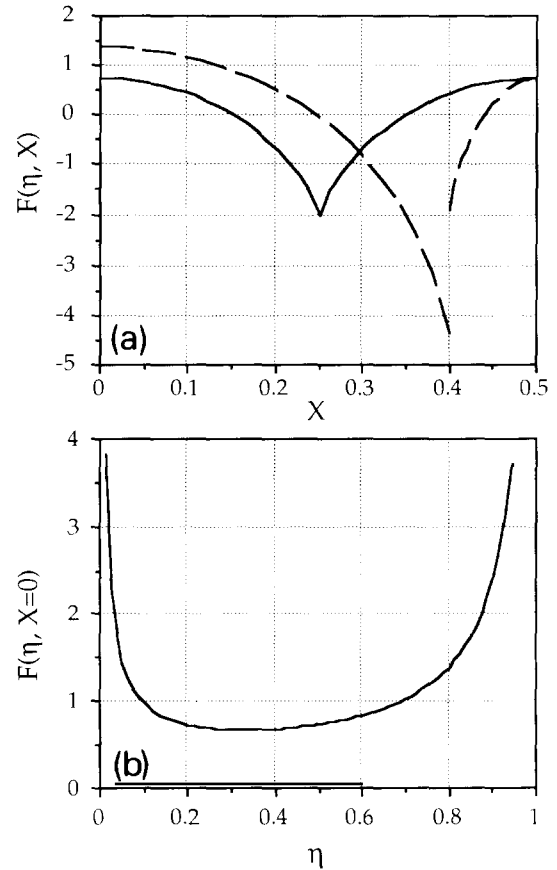


Fig. 15. (a) Plot of the function $F(\eta, X)$ appearing in the JH approximate expression for the concentration field, for $\eta = 0.5$ (solid line) and 0.8 (broken line). (b) $F(\eta, X = 0)$ as a function of η .

where

$$\langle \Delta T \rangle_1 = \frac{2\overline{m_\alpha m_\beta} \Delta C}{(m_\alpha + m_\beta) \eta_\alpha \eta_\beta} \frac{\lambda_{scal}}{l_{diff}} \left(\frac{\lambda}{\lambda_{scal}} + \frac{\lambda_{scal}}{\lambda} \right), \quad (A.4)$$

$$\langle \Delta T \rangle_2 = \frac{\eta_\alpha m_\alpha - \eta_\beta m_\beta}{m_\alpha - m_\beta} G \lambda (Z_{j,\beta} - Z_{j,\alpha}). \quad (A.5)$$

Eq. (A.4) is the formula given by Jackson and Hunt [2] and eq. (A.5) the correction following from the removal of the equal average-undercooling ansatz. While the minimum of $\langle \Delta T \rangle_1$ occurs,

independently of G , at $\lambda/\lambda_{scal} = 1$, the value $\lambda_{min}/\lambda_{scal}$ minimizing $\langle \Delta T \rangle$ is a function of Γ . In the limit $\Gamma \rightarrow \infty$, it is shown, in ref. [27], that

$$(\lambda_{min})^2 = 2 \frac{m_\alpha d_\alpha \sin(\theta_\alpha) + m_\beta d_\beta \sin(\theta_\beta)}{m_\alpha U(\eta_\alpha) + m_\beta U(\eta_\beta)}, \quad (A.6)$$

where the function U (see fig. 14) is defined by:

$$U(\eta) = P(\eta) - \frac{\eta}{2} P'(\eta). \quad (A.7)$$

In fig. 16, the ratio $\lambda_{min}/\lambda_{scal}$ calculated from eqs. (A.6) and (A.7) is plotted (i) as a function of η_α , for $V = 0.27 \mu m s^{-1}$ and $G = 80 K cm^{-1}$; (ii) as a function of V , for $A = 1$, $G = 80 K cm^{-1}$ and two different values of η_α .

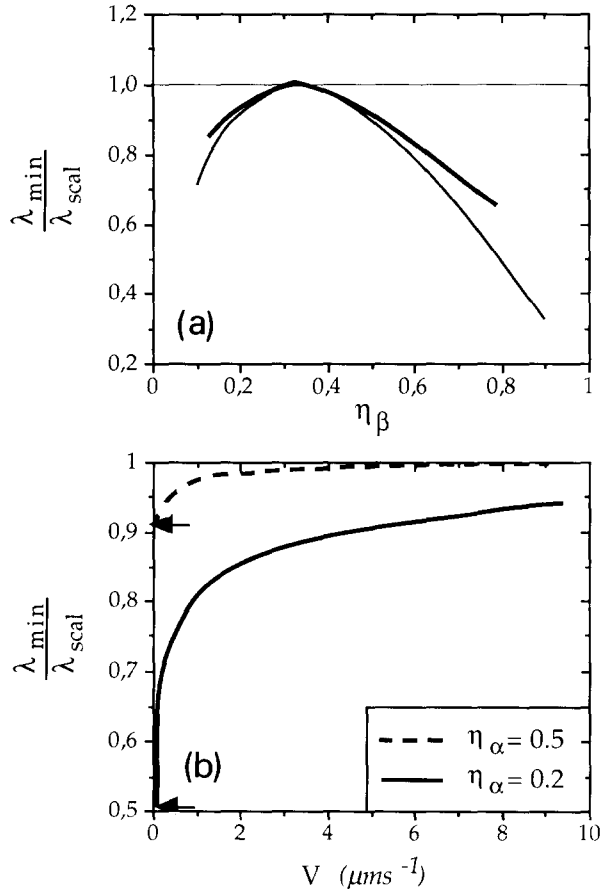


Fig. 16. Relative departure of λ_{min} from λ_{scal} : (a) as a function of η_β (bold line: $V = 0.27 \mu m s^{-1}$ and $G \approx 30 K cm^{-1}$; thin line: $\Gamma = \infty$; broken line: fictitious symmetrical alloy and $\Gamma = \infty$); (b) as a function of V , for $G \approx 30 K cm^{-1}$ and the values of η_α given in the insert (arrows: $\Gamma = \infty$).

Acknowledgements

We gratefully acknowledge numerous stimulating and enlightening discussions with B. Caroli and C. Caroli. Thanks are due to S. de Cheveigné for her contribution to the analysis of the images. We are indebted to C. Misbah, K. Kassner and S. Akamatsu for the communication of unpublished results. This research was supported by the CNRS and the CNES. During this work, J. Mergy was financially supported by the Société Pétichiney.

References

- [1] J.D. Hunt and K.A. Jackson, Trans. AIME 236 (1966) 843.
- [2] K.A. Jackson and J.D. Hunt, Trans. AIME 236 (1966) 1129.
- [3] W. Kurz and D.J. Fischer, Fundamentals of Solidification (Trans Tech, Aedermannsdorf, 1984).
- [4] B. Caroli, C. Caroli and B. Roulet, in: Solids Far from Equilibrium, Ed. C. Godrèche (Cambridge University Press, 1992).
- [5] K.A. Jackson and J.D. Hunt, Acta Met. 13 (1965) 1212.
- [6] W.L. Kaukler, PhD Thesis, University of Toronto (1981).
- [7] W.L. Kaukler and J.W. Rutter, in: In Situ Composites, Eds. F.D. Lemkey, H.E. Cline and M. McLean (Elsevier, Amsterdam, 1982) p. 30.
- [8] W.L. Kaukler and J.W. Rutter, Mater. Sci. Eng. 65 (1984) L1.

- [9] V. Seetharaman and R. Trivedi, *Met. Trans.* 19A (1988) 295.
- [10] G. Faivre, S. de Cheveigné, C. Guthmann and P. Kurowski, *Europhys. Letters* 9 (1989) 779.
- [11] B. Caroli, C. Caroli, G. Faivre and J. Mergy, *J. Crystal Growth* 118 (1992) 135.
- [12] G. Faivre, C. Guthmann and J. Mergy, in: *Nonlinear Phenomena in Materials Science*, Vol. 2, Eds. L. Kubin and G. Martin (Trans Tech, Aedermannsdorf, 1992).
- [13] G. Faivre and J. Mergy, *Phys. Rev. A* 45 (1992) 7320; *A* 46 (1992) 963.
- [14] J. Mergy, Thèse, Université Paris 7 (1992).
- [15] W. Blitz und E. Meinecke, *Z. Anorg. Allg. Chem.* 131 (1923) 1.
- [16] A. Pavlovskaya and D. Nenow, *Kristall Tech.* 11 (1976) 235; 12 (1977) 473.
- [17] A. Pavlovskaya and D. Nenow, *J. Crystal Growth* 39 (1977) 346.
- [18] R.M. Gutowski and W.R. Wilcox, *Separation Sci. Technol.* 15 (1980) 39.
- [19] S. de Cheveigné, C. Guthmann and M.M. Lebrun, *J. Physique* 47 (1986) 2095; see also M.M. Lebrun, Thèse, Université Paris 7 (1987).
- [20] J.M. Laherrere, R. Mellet, H. Savary, C. Licoppe, J.F. Scott and J.C. Toledano, *Phys. Rev. A* 42 (1990) 3434; see also: J.M. Laherrere, Thèse, Université Paris 6 (1990).
- [21] P.E. Cladis, J.T. Gleeson and P.L. Finn, in: *Patterns and Instabilities*, Eds. D. Walgraef and N. Ghoniem (Kluwer, Dordrecht, 1990).
- [22] W.W. Mullins and R.F. Sekerka, *J. Appl. Phys.* 35 (1964) 444.
- [23] W.A. Tiller, K.A. Jackson, J.W. Rutter and B. Chalmers, *Acta Met.* 1 (1953) 498; see also: V.G. Smith, W.A. Tiller and J.W. Rutter, *Can. J. Phys.* 33 (1955) 723.
- [24] Eq. (2) corresponds to the first term of a development in $k_c l_{\text{diff}}$ (k_c : marginal wavevector; see ref. [4]). The next term in the development can be taken into account as a correction on l_{th} . This correction, of order 10%, has been applied to the results shown in fig. 5.
- [25] K. Kassner and C. Misbah, *Phys. Rev. A* 44 (1991) 6513.
- [26] K. Kassner and C. Misbah, *Phys. Rev. Letters* 66 (1991) 445.
- [27] K. Brattkus, B. Caroli, C. Caroli and B. Roulet, *J. Physique* 51 (1990) 1847.
- [28] R.L. Cormia, F.P. Price and D. Turnbull, *J. Chem. Phys.* 37 (1962) 1333.
- [29] B. Caroli, C. Caroli and B. Roulet, *J. Physique* 51 (1990) 1865.
- [30] R. Trivedi, J.T. Mason, J.D. Verhoeven and W. Kurz, *Met. Trans.* 22A (1991) 2523.